J. Fluid Mech. (1986), *vol.* 166, *pp.* 139–159
Printed in Great Britain

Particle motions induced by spherical convective elements in Stokes flow

By R. W. GRIFFITHS

Research School of Earth Sciences, The Australian National University,
G.P.O. Box 4, Canberra, A.C.T. 2601, Australia

(Received 30 June 1985 and in revised form 11 November 1985)

The motions of fluid particles within and around a mass of hot, buoyant material (a thermal) rising through an extremely viscous, unbounded environment are computed using a simple kinematic model. The model is based on a similarity solution by Griffiths (1986*a*) and allows for growth of thermals due to outward diffusion of heat. Particle motions are also computed for the case of a non-expanding, isothermal sphere, such as a bubble of relatively low-viscosity fluid, in Stokes flow. Motions induced in the surroundings lead to large vertical displacements: the 'total drift' function and hydrodynamic mass corresponding to those defined for the inviscid case by Darwin (1953) and Lighthill (1956) are infinite in this unbounded geometry. Rotation of initially horizontal fluid elements (strain) in the surroundings is discussed.

All material lying within an expanding thermal becomes confined at later times to a torus (dye ring) if the Rayleigh number for the thermal is large, to a central tapered blob if $Ra < 50$, or to an umbrella-shaped cap with narrow stem if Ra takes intermediate values. The 'mushroom' shape widely observed for tracers within laminar elements in thermal convection is predicted for intermediate-to-large Rayleigh numbers. Buoyancy and heat, on the other hand, are assumed to remain evenly distributed throughout an enlarging sphere. Laboratory experiments illustrate and confirm the predictions of the model.

1. Introduction

Injection of a fixed quantity of heat, or of a volume of hot fluid, into an otherwise uniform viscous fluid leads to buoyant convection that is characterized by a small Reynolds number ($Re \ll 1$) when the ambient viscosity is large or the injected buoyancy small. In laboratory experiments Griffiths (1986*a*), hereafter referred to as I, showed that for small Reynolds numbers the buoyant material always forms an approximately spherical thermal which rises at Stokes' terminal velocity. Using this velocity, the Reynolds number $Re = UD/\nu_\infty$, (where U is the translation speed, D is the sphere diameter and ν_∞ is the ambient kinematic viscosity) may be written in terms of the total buoyancy $B = g\Delta\rho V/\rho_\infty$ (V the sphere volume, $\Delta\rho$ the density difference and g the gravitational acceleration), so that $Re = B/2\pi\nu_\infty^2$. A second parameter describing the flow is the Rayleigh number $Ra = B/\kappa\nu_\infty$, where κ is the diffusivity for heat. Then the flow has small Reynolds number if $Ra \ll 2\pi Pr$, where $Pr = \nu_\infty/\kappa$ is the Prandtl number for the surrounding fluid.

As thermals rise they enlarge as a result of outward diffusion of heat and associated buoyancy. If the advective timescale is long compared to the diffusive timescale ($Ra \ll 1$), heat diffuses radially in all directions until the thermal anomaly is

dissipated (Morton 1960). If the advective timescale is small compared to that for diffusion ($Ra \gg 1$), the outer edge of the thermal is a thin boundary layer containing newly heated material from the surroundings (I). This boundary-layer material is hot and buoyant and therefore takes part in the rising motion. It was argued in I that almost all of the heated material will be incorporated into the thermal, implying that thermals entrain mass while conserving their buoyancy in the same manner as turbulent inviscid thermals (Scorer 1957, 1978; Turner 1957, 1973). Conservation of buoyancy and an assumption of self-similar flow lead to the prediction that thermals will expand linearly with distance travelled: $D - D_0 = 2\epsilon(z - z_0)$, where D_0 and z_0 are an initial diameter and position and the half-angle of expansion $\phi = \tan^{-1}\epsilon$ is related to the Rayleigh number according to $\epsilon \sim Ra^{-\frac{1}{2}}$. Both the linear expansion and dependence of ϵ on Ra were confirmed by laboratory experiments in the range $250 < Ra < 25000$. The semi-empirical expansion rate is

$$\epsilon = (1.25 \pm 0.2)\, Ra^{-\frac{1}{2}}. \tag{1}$$

As a thermal expands, the velocity decreases with time according to $U \sim t^{-\frac{1}{2}}$ so that the viscous drag can continue to balance the constant driving force. Expansion also implies that the initial buoyant fluid occupies only a fraction of the volume of the thermal at later times.

The displacements of fluid particles in low Reynolds-number flow are of interest. Particle motions determine the patterns into which passive tracers (dye or chemical heterogeneities) are shaped by thermal convection or by the passage of buoyant bodies. Similarly, distortions (strain) in the viscous surroundings can be found by integrating relative motions through time. Such relative motions have not previously been discussed even for the case of steady isothermal Stokes flow past a rigid sphere or bubble of low-viscosity fluid. In a geological context, distortions are found within the layered rocks of the Earth's crust adjacent to large intrusive masses of magma and salt domes (Ramberg 1981; Schwerdtner 1982). Furthermore, both non-expanding bodies and expanding convective elements must cause large displacements of the surrounding fluid in the direction of motion as a result of viscous drag. These displacements represent a stirring which, in the presence of molecular diffusion or externally imposed velocity shear, can contribute to vertical mixing.

For the case of motion of a sphere through an inviscid fluid, Maxwell (1870), Darwin (1953), Lighthill (1956) and Yih (1985) discussed the displacement of fluid particles in the surroundings. Displacements can be described by a 'total drift function' that predicts a finite movement for particles initially lying a finite distance off the axis of motion as the body is displaced through an infinite distance. The drift function leads to a finite drift mass, which by Darwin's theorem is equal to the added mass, the difference between the virtual (hydrodynamic) mass and the real mass of the body. These quantities are finite as a result of the rapid decrease of irrotational velocities with distance from the sphere. For expanding inviscid thermals, Turner (1964) investigated the motions of fluid particles both inside and outside the rising mass of well-mixed buoyant fluid. The flow outside the thermal at any instant in time was taken to be identical to potential flow about a solid sphere translating at an arbitrary constant velocity. Flow inside the thermal was assumed to take the form of Hill's spherical vortex, with inner and outer velocities matched at the edge of the thermal. Entrainment causes a slow enlargement of the radius of the sphere, a time-dependence that was incorporated into numerical integrations of particle velocities to find particle

paths. Some particles initially far ahead of the thermal then enter the spherical vortex. For small rates of expansion, these particles lie within a cone ahead of the thermal and symmetric about the axis of motion. If the half angle of expansion exceeds a critical value all of the surrounding fluid is eventually incorporated into the sphere. At all angles of expansion the total drift of particles is infinite.

A kinematic model, similar to that formulated by Turner (1964) for the inviscid case, is presented here for motions induced by expanding extremely viscous thermals. The model relies to some extent on the dynamical model in I. Particle paths and distortions of passive material surfaces in the environment are predicted, and compared where possible with those observed in laboratory experiments in which isolated thermals are produced. Corresponding exact results for a non-expanding isothermal sphere (which may be rigid or simply a fluid of different intrinsic density) in Stokes flow are also presented. Some of the experiments shown are taken from among those discussed in I, while others are additional runs using the same apparatus and techniques.

2. Relative motion about a viscous thermal

Only thermals with large Rayleigh numbers ($Ra \gg 1$) and extremely small Reynolds numbers ($Re \ll 1$) are considered, and we recall from I that under this condition diffusion of heat maintains a thin thermal boundary layer in the surrounding fluid. We assume that all the material entering the thermal boundary layer is entrained into the thermal and that the combination of circulation and diffusion maintains a uniform temperature (and viscosity) throughout the buoyant fluid. In its steady or only very slowly varying form, it is assumed here that the buoyant fluid maintains a spherical shape, as this appears to be the only steady solution for creeping flow (Kojima, Hinch & Acrivos 1984) and is that observed in the experiments (I).

Since thermals expand only slowly in time the streamfunction for flow around a thermal is given by the steady flow about a non-expanding sphere. This argument becomes exact when the Reynolds number is small, since time dependent terms in the momentum equation vanish. In a spherical polar coordinate system moving with the centre of the thermal the boundary of the buoyant fluid is placed at $r = a$, with $\theta = 0$ the (vertical) direction of motion. The stream function for flow outside the thermal is given by

$$\psi_2 = \tfrac{1}{2}Ur^2 \sin^2\theta\left[\left(\frac{a}{r}-\frac{a^3}{r^3}\right)\left(\frac{\mu_2+\frac{3}{2}\mu_1}{\mu_2+\mu_1}\right)+\frac{a^3}{r^3}-1\right] \quad (r > a), \tag{2}$$

and the circulation inside the thermal is given by the spherical vortex

$$\psi_1 = \tfrac{1}{4}Ur^2 \sin^2\theta\left(1-\frac{r^2}{a^2}\right)\left(\frac{\mu_2}{\mu_2+\mu_1}\right) \quad (r < a), \tag{3}$$

where ψ is Stokes streamfunction, μ is the dynamic viscosity (assumed uniform in each domain), and subscripts 1 and 2 refer to the inner and outer regions, respectively (Lamb 1932). The velocity at $r = a$ is continuous. No assumption about the form of the interior flow is needed, other than that the flow there is laminar, contains no significant density differences, and that the velocity and stress are continuous at the

spherical interface†. From (2) and (3) the instantaneous velocity components for a fluid particle become

$$\left.\begin{aligned} v_r &= U\cos\theta\left[\left(\frac{a}{r}-\frac{a^3}{r^3}\right)\left(\frac{\mu_2+\frac{3}{2}\mu_1}{\mu_2+\mu_1}\right)+\frac{a^3}{r^3}-1\right] \\ v_\theta &= -U\sin\theta\left[\frac{1}{2}\left(\frac{a}{r}+\frac{a^3}{r^3}\right)\left(\frac{\mu_2+\frac{3}{2}\mu_1}{\mu_2+\mu_1}\right)-\frac{a^3}{2r^3}-1\right] \end{aligned}\right\} \quad (r>a), \tag{4}$$

$$\left.\begin{aligned} v_r &= \tfrac{1}{2}U\cos\theta\left(1-\frac{r^2}{a^2}\right)\left(\frac{\mu_2}{\mu_2+\mu_1}\right) \\ v_\theta &= -\tfrac{1}{2}U\sin\theta\left(1-\frac{2r^2}{a^2}\right)\left(\frac{\mu_2}{\mu_2+\mu_1}\right) \end{aligned}\right\} \quad (r<a). \tag{5}$$

The similarity solution and experimental results in I show that the radius a, the height of rise z above a virtual origin $z=0$, and velocity U of a thermal obey the forms

$$a=\epsilon z, \quad z=mt^{\frac{1}{2}}, \quad U=\tfrac{1}{2}mt^{-\frac{1}{2}}, \tag{6}$$

where t is the time since the thermal was centred at the virtual origin, ϵ and m are constants, and (as in 1) ϵ is the tangent of the half angle of spread. Note that $a=0$ at the virtual origin.

In order to explicitly include the time dependence of the flow and to calculate the paths of fluid particles or tracers relative to the thermal, the motion can be transformed into a coordinate system that is both at rest relative to the centre of the sphere (as in (2)–(5)) and expanding with the radius of the sphere. A dimensionless radius in this coordinate system, using (6), is

$$\eta=\frac{r}{a}=\frac{r}{\epsilon m t^{\frac{1}{2}}}. \tag{7}$$

Substituting (7) into (4) and (5), with $v_r=\mathrm{d}r/\mathrm{d}t$, $v_\theta=r\,\mathrm{d}\theta/\mathrm{d}t$ and U as given by (6), yields the particle velocities

$$\left.\begin{aligned} \frac{\mathrm{d}\eta}{\mathrm{d}t} &= \frac{-1}{2\epsilon t}\left\{\epsilon\eta+\cos\theta\left[\left(1-\frac{1}{\eta^3}\right)-\left(\frac{1}{\eta}-\frac{1}{\eta^3}\right)\left(\frac{1+\frac{3}{2}\mu_1/\mu_2}{1+\mu_1/\mu_2}\right)\right]\right\} \\ \frac{\mathrm{d}\theta}{\mathrm{d}t} &= \frac{\sin\theta}{2\epsilon t\eta}\left[\left(1+\frac{1}{2\eta^3}\right)-\tfrac{1}{2}\left(\frac{1}{\eta}+\frac{1}{\eta^3}\right)\left(\frac{1+\frac{3}{2}\mu_1/\mu_2}{1+\mu_1/\mu_2}\right)\right] \end{aligned}\right\} \quad (\eta>1), \tag{8}$$

$$\left.\begin{aligned} \frac{\mathrm{d}\eta}{\mathrm{d}t} &= \frac{1}{2\epsilon t}\left[-\epsilon\eta+\tfrac{1}{2}(1-\eta^2)\frac{\cos\theta}{(1+\mu_1/\mu_2)}\right] \\ \frac{\mathrm{d}\theta}{\mathrm{d}t} &= \frac{\sin\theta}{4\epsilon t\eta}\frac{(2\eta^2-1)}{(1+\mu_1/\mu_2)} \end{aligned}\right\} \quad (\eta<1). \tag{9}$$

The radial velocities in (8) and (9) are a superposition of a radial flow toward a sink at the origin and the radial component of flow about a non-expanding sphere, adjusted to account for the fact that a constant velocity in non-expanding coordinates corresponds to a continuously decreasing velocity in the enlarging system. As well as the viscous terms, the factor of 2 in the denominators of (8) and (9) does not appear

† In the turbulent inviscid case the form of the spherical vortex must be assumed. In that case, the stream function for the exterior irrotational flow includes only the last two terms inside the brackets in (2).

in Turner's (1964) relations for the inviscid case because he assumed a constant velocity $U = 1$: his velocities in the expanding frame are halved when the time-dependence of the translation speed ($U \sim t^{-\frac{1}{2}}$) is included.

A particle can be followed through time and space, starting from any chosen initial position (η_0, θ_0, t_0), by integrating either set (8) or (9) of two coupled first-order differential equations, depending on whether the particle lies inside or outside the boundary $\eta = 1$. If the particle passes through $\eta = 1$ the integration must change to the opposite set, beginning with initial conditions provided by the final values from the previous integration to $\eta = 1$.

For the case $\epsilon = 0$, the sphere is not expanding and the flow is truly steady. Particle paths are then streamlines in the non-expanding coordinates, lines of constant ψ given by (2) and (3). Particle positions can then be found as functions of time by numerically integrating (4) and (5).

3. Numerical solutions

3.1. *Presentation of results*

In order to construct the pattern of particle motions relative to an expanding sphere, (8) and (9) were integrated for a number of initial conditions, giving the paths of a number of particles. Because the flow is weakly dependent on the ratio of viscosities, the two cases $\mu_1/\mu_2 = 1$ and $\mu_1/\mu_2 = 0$ were selected for study. The latter case is of interest because most fluids with very large Prandtl numbers are also characterized by strongly temperature-dependent viscosities: fluid inside a hot thermal often has $\mu_1 \ll \mu_2$. The same limit is also relevant for non-expanding isothermal spheres (bubbles) in which a large viscosity difference is often associated with the compositional difference that drives the motion. Results for $\mu_1/\mu_2 \to \infty$ (a rigid sphere) are not shown here but are not greatly different from those for $\mu_1 = \mu_2$. The model for expanding thermals is not valid when $\mu_1 \gg \mu_2$ because the heated boundary layer cannot enter the slow or stagnant spherical vortex, and must instead accumulate behind the thermal, destroying the spherical geometry.

Figures 1, 2 and 3 show the results for expansion rates of $\epsilon = 0.03$; 0.10 and 0.24, respectively. These values of ϵ are chosen as strategic values illustrating the possible flow regimes. For each particle, integration began at (x_0, y_0) and $t_0 = 1$, where the rectangular coordinates (x, y) have $x = 0$ on the vertical axis of motion and $y = 0$ on the horizontal plane through the centre of the sphere. The top of each figure corresponds to the chosen value of y_0 in sphere radii ($y_0 = 5$). However, the computed paths show a negligible dependence on y_0 of the computed paths once $y_0 \geqslant 10$, and only small variations for $y_0 \geqslant 5$. The paths of selected particles are plotted on the right-hand side of each figure, with dots showing time intervals that are of equal length *on a square-root scale*. Thus two adjacent dots near the beginning of a trajectory show a time interval much shorter than that between two dots near the end of the trajectory. On the left side of each figure, a similar integration was carried out for a large number of particles (typically 500) initially distributed along $y = y_0$, and their positions at chosen times connected to show the successive shapes of a material surface. Only for the largest expansion rate does the virtual origin lie within the area shown (figure 3). The virtual origin is the point in space at which the expanding thermal is to be found when its diameter is zero, and is the point toward which all particle paths far from the thermal are directed in our expanding coordinate frame. If we consider all fluid below an initially horizontal material surface to be tagged with a tracer such as dye, then the area in which that tracer is found at large times (long

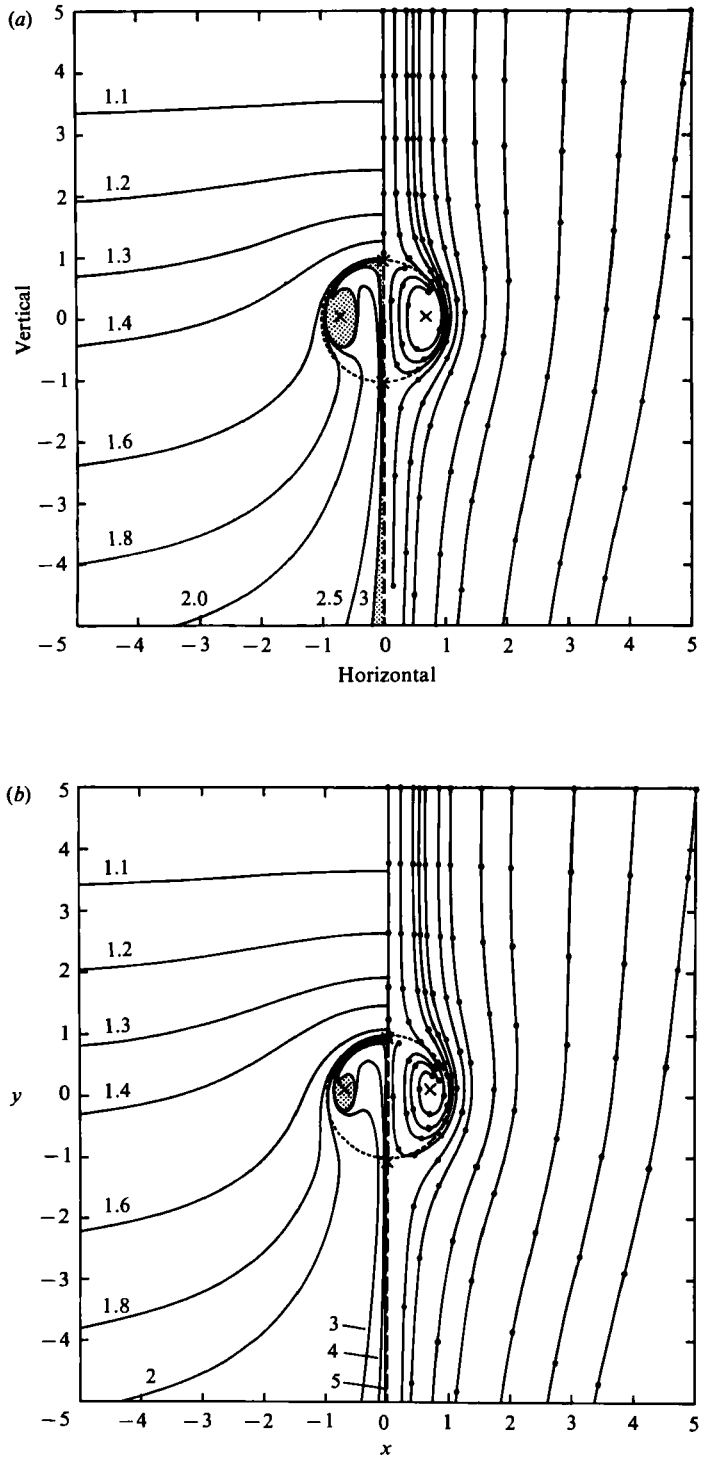

FIGURE 1 (*a*, *b*). For caption see facing page.

after the thermal passes through the initial level of the surface) is that shaded on figures 1, 2 and 3.

Figure 4 shows particle trajectories and distortions of material surfaces for a non-expanding sphere with $\mu_1/\mu_2 = 0$. Since the sphere in this case travels at a constant terminal velocity U, dots on each path show ten *equal intervals* of time, and the material surface is shown at times $2.5a/U$ apart.

3.2. *Stagnation points*

The shapes of particle paths are dependent upon the location of stagnation points. There are, in general, one stagnation point and a stagnation circle inside an expanding sphere. From (9) both radial and azimuthal velocities vanish at $\eta = 0$ when $\epsilon = \infty$, which is the trivial case of no motion in the non-expanding reference frame, resulting from an infinite exterior viscosity or infinitely rapid diffusion of heat away from the sphere. The azimuthal velocity also vanishes at $\theta = 0, \pi$ and at $\eta = 1/\sqrt{2}$. The radial velocity is zero when

$$\epsilon\eta - \tfrac{1}{2}(1-\eta^2)\, k \cos\theta = 0, \tag{10}$$

where $k = \mu_2/(\mu_2+\mu_1)$. Solving the quadratic (10) at $\theta = 0$ implies a stagnation point at

$$\eta = \frac{-\epsilon}{k} \pm \left(\frac{\epsilon^2}{k^2}+1\right)^{\frac{1}{2}} \quad (\theta = 0), \tag{11}$$

where only the positive sign is meaningful; the negative sign yields negative values of η. Hence the forward stagnation point (see figures 1–4) lies between $\eta = 1$ for $\epsilon = 0$ and $\eta \to 0$ for $\epsilon \to \infty$. When $\theta = \pi$, the solution to (10) for all $\epsilon > 0$ gives $\eta > 1$, a domain in which the interior streamfunction is not valid.

On the surface $\eta = 1/\sqrt{2}$, where $\mathrm{d}\theta/\mathrm{d}t = 0$, (10) predicts a circular stagnation line at

$$\cos\theta = 2\sqrt{2}\epsilon\left(1+\frac{\mu_1}{\mu_2}\right) \quad (\eta = 1/\sqrt{2}). \tag{12}$$

In the non-expanding case ($\epsilon = 0$), this circle lies on the horizontal plane through the centre of the sphere ($\theta = \pm\frac{1}{2}\pi$). At finite expansion rates the stagnation circle (12) lies farther toward the front of the thermal. This position also lies farther forward for larger viscosity ratios. At a well-defined value of ϵ the circle coalesces with the forward axial stagnation point (11): the stagnation circle exists only for $\epsilon < [2\sqrt{2}(1+\mu_1/\mu_2)]^{-1}$. This critical expansion ratio is $\epsilon^* \approx 0.354$ when $\mu_1/\mu_2 = 0$ and $\epsilon^* \approx 0.177$ when $\mu_1/\mu_2 = 1$†.

† The corresponding condition in the inviscid case can be shown to be $\epsilon < 3/2\sqrt{2} = 1.061$.

FIGURE 1. (*a*) Particle motions, plotted in the expanding coordinate frame, relative to an expanding spherical vortex with $\epsilon = 0.03$ and $\mu_1/\mu_2 = 0$. Vertical and horizontal scales are in sphere radii. Particles have $y_0 = 5$ at the time $t_0 = 1$, and paths on the right-hand side are shown up to $t = 3.0$, with dots at equal intervals in $t^{\frac{1}{2}}$. Material surfaces are drawn on the left for the times shown, again starting at $y_0 = 5$ at $t_0 = 1$. Crosses show stagnation points in the expanding coordinate system. Dotted line is the surface of the sphere. Broken line is the axis of symmetry. Stippled region is that in which fluid initially below the horizontal material surface is found at $t = 3.0$, and is approximately the region in which the injected dyed fluid will be found in the experiments. (*b*) As for (*a*) but for $\epsilon = 0.03$ and $\mu_1/\mu_2 = 1$. Particle paths on the right are shown up to time $t = 5.0$. Stippled region is as in (*a*) but for $t = 5$.

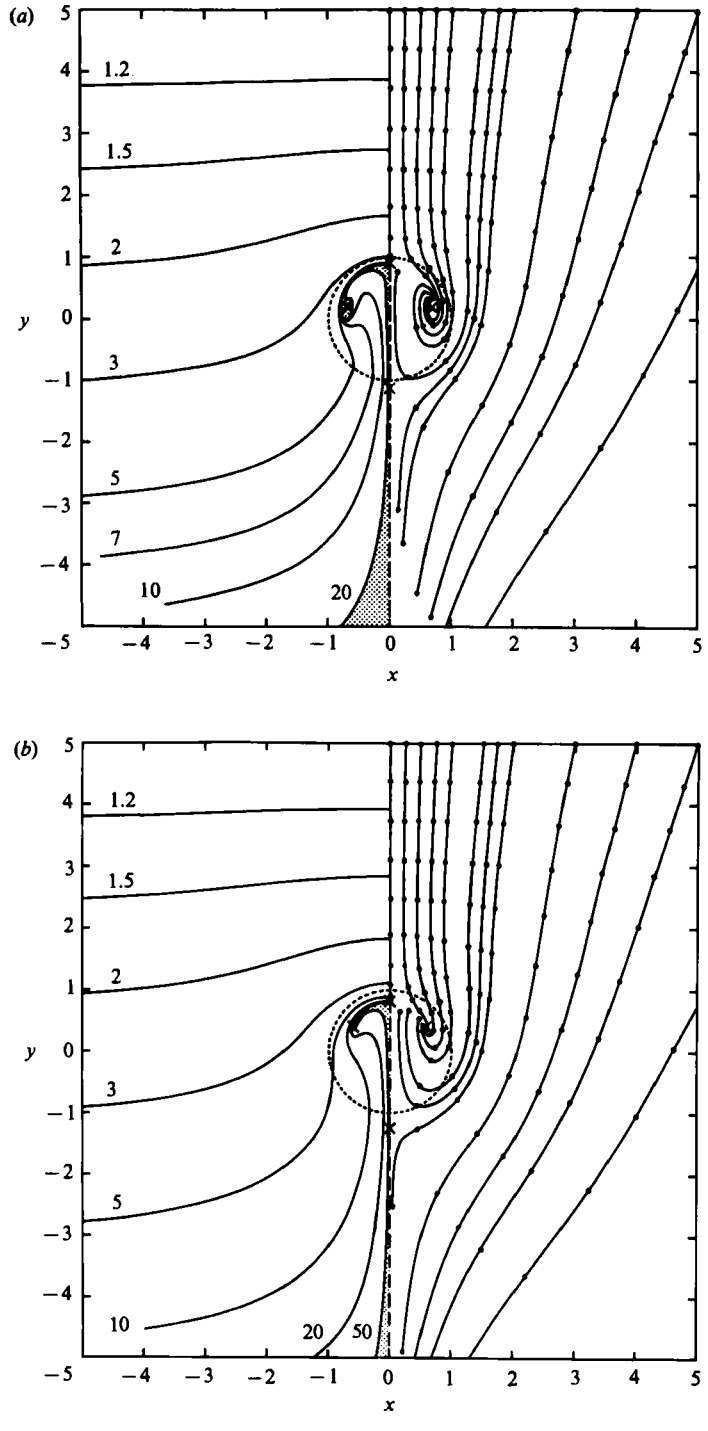

FIGURE 2. (*a*) Particle motions in the expanding coordinate system for an expanding sphere with $\epsilon = 0.10$ and $\mu_1/\mu_2 = 0$. Initial conditions for each particle are $y_0 = 5$, $t_0 = 1$ and x_0 as seen by the positions of particles at the top of the figure. Paths are shown up to $t = 20$, and the stippled region is for $t = 20$. Other details are as in figure 1 (*a*). (*b*) As for (*a*) but for $\epsilon = 0.10$ and $\mu_1/\mu_2 = 1$. Particle paths and material surfaces are computed up to $t = 50$.

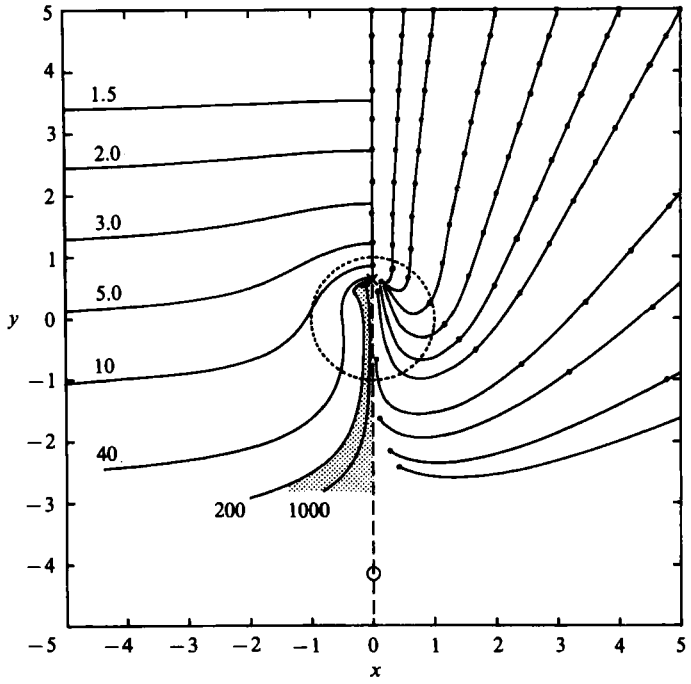

FIGURE 3. Particle paths (right) and material surfaces (left) for an expanding sphere with $\epsilon = 0.24$, $\mu_1/\mu_2 = 1$. Stippled region shows the location at $t = 200$ of fluid from below the material surface that was horizontal at $y_0 = 5$, $t_0 = 1$. The small circle on the axis shows the position of the virtual origin. Other details are as in figure 1(*a*). Results for $\epsilon = 0.24$, $\mu_1/\mu_2 = 0$ are not shown as they are largely similar to those in figure 2(*b*).

Stagnation points outside the sphere are found by setting $\mathrm{d}\eta/\mathrm{d}t = \mathrm{d}\theta/\mathrm{d}t = 0$ in (8). Here, $\mathrm{d}\theta/\mathrm{d}t = 0$ only at $\theta = 0, \pi$. For $\theta = 0$ the radial velocity vanishes only at $\eta = 1$, $\epsilon = 0$. For $\theta = \pi$, the radial velocity vanishes at the roots of the quartic

$$\epsilon\eta^4 - \eta^3 + \left(\frac{\mu_2 + \frac{3}{2}\mu_1}{\mu_2 + \mu_1}\right)(\eta^2 - 1) + 1 = 0. \tag{13}$$

Numerical solution of (13) shows that for small values of ϵ, there are two roots at $\eta \geqslant 1$. These are plotted on figure 5 for the two cases $\mu_1/\mu_2 = 0, 1$, along with the position of the virtual origin. Since ϵ is the tangent of the half-angle of spread, the virtual origin lies at $y = -1/\epsilon$, where y is the vertical coordinate in sphere radii relative to the centre of the sphere. At $\epsilon = 0$ there is only one stagnation point behind the thermal: at $y = -1$. For $\epsilon > 0$, this stagnation point lies a small distance behind the sphere and a second lies above the virtual origin. If no sphere was present in the flow, particle velocities in the expanding coordinate system would approach zero at the virtual origin. However, the presence of a sphere decreases the downward velocities everywhere below the sphere, causing the axial velocity to vanish at a new stagnation point above the virtual origin. Close to the virtual origin, particles move toward the sphere. At large values of ϵ, the two rear stagnation points approach each other until they coalesce at $\epsilon = \epsilon'(\mu_1/\mu_2)$. There are no stagnation points behind the sphere for $\epsilon > \epsilon'$, implying that flow is everywhere directed toward the sphere and that all of the surroundings eventually enter the spherical vortex. For $\mu_1/\mu_2 = 0$, $\epsilon' = 0.251$, and for $\mu_1/\mu_2 = 1$, $\epsilon' = 0.207$†.

† The corresponding value for the inviscid case is $\epsilon' = 0.47$ (Turner 1964).

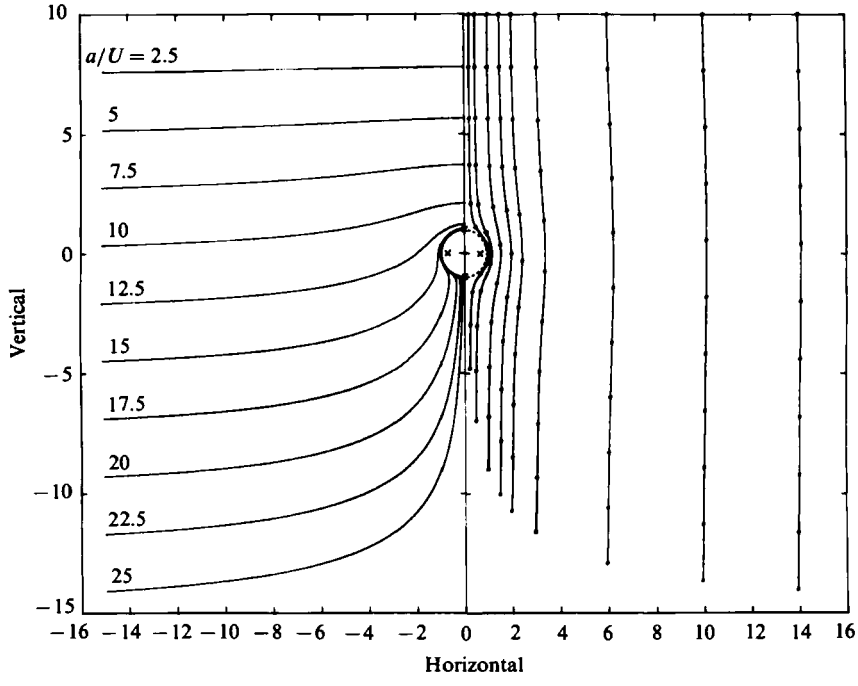

FIGURE 4. Particle paths and positions of a material surface relative to a sphere as computed from the exact solution for Stokes flow about a non-expanding sphere ($\epsilon = 0$). Initial conditions for each integration were $y_0 = 10$, $t_0 = 0$. Dots on particle paths show equal intervals in time and times for material lines are shown in units of a/U. The displacements of material lines at $x = |15|$ from their initial positions in a stationary reference frame are shown by the mismatch with the scale on the vertical axis (e.g. at $a/U = 20$, the displacement is $0.7a$). Crosses show stagnation points for the flow.

3.3. *Implications of particle paths*

Far ahead of an expanding spherical vortex, particles move in straight lines toward the virtual origin, as they would if no sphere were present. Their paths subtend an angle β to the vertical, where $\tan\beta = \epsilon x_0/(\epsilon y_0 + 1)$. However, the straight paths are disturbed as particles approach the sphere. Those close to the axis enter the spherical vortex, while particles farther from the axis are slowed down but continue on toward the virtual origin. The path dividing those that enter from those that do not approaches the first rear stagnation point, and this dividing path subtends a larger angle β^* to the axis for larger expansion ratios ϵ (figures 1–4). In other words, particles destined to enter the sphere originate within a cone whose vertex is the virtual origin. The half-angle β^* of the cone of entrainment, along with the corresponding values computed by Turner (1964) for the inviscid case, is plotted on figure 6. For $\epsilon < 0.1$, the numerical results are consistent with $\tan\beta^* \approx b\epsilon^{1.6}$, where $b \approx 4.0$ for $\mu_1/\mu_2 = 0$ and $b \approx 4.7$ for $\mu_1/\mu_2 = 1$. Thus for small expansion ratios the cone of material destined to be incorporated into a thermal subtends a smaller angle at the virtual origin than does the thermal itself ($\tan\beta^* < \epsilon$). This is possible simply because the sphere, for small ϵ, must at any time contain a volume approximately equal to the volume of the entrainment cone between the virtual origin and the level of the sphere. On the other hand, for large ϵ much of the mass in the entrainment cone at levels

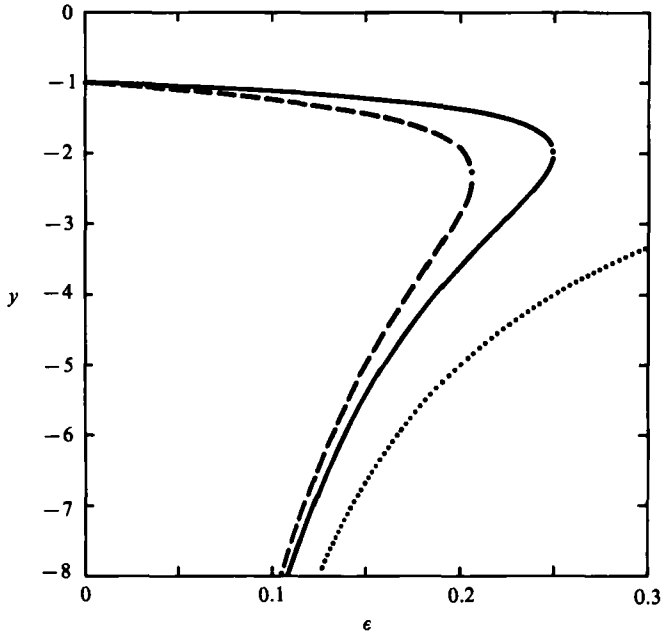

FIGURE 5. The position (in sphere radii) of axial stagnation points behind expanding spheres with $\mu_1/\mu_2 = 0$ (solid line) and $\mu_1/\mu_2 = 1$ (broken line) as functions of the expansion ratio. The dotted curve shows the position of the virtual origin. Upper and lower branches of each curve correspond to two stagnation points that approach each other as ϵ increases, coalescing at the position shown with a dot.

below the sphere at a given time has not entered the sphere, though it will do so eventually.

Comparison of the particle motions on figures 1–4 shows that particles take longer to reach the sphere, and the overturning time for the spherical vortex is longer, for larger expansion ratios and larger viscosity ratios (for which the sphere velocity U decreases more rapidly). Distortion of material surfaces becomes significant in all cases once the surface has been advected to within about three radii from the centre of the sphere. Surfaces stretch as they move past the sphere, and become wrapped around in the spherical vortex. Behind the sphere they form a large funnel that represents the total vertical displacement of fluid particles in the environment (see §4).

Within the spherical vortex for small expansion ratios (figure 1), the entrained material surfaces eventually form the outline of a torus or dye ring, a thin cap over the forward edge of the sphere, and a thin vertical stem along the axis behind the thermal. The dye ring decreases in sectional area with time in order to maintain a constant volume (in non-expanding coordinates) as the sphere expands. The radius of the dye ring as measured normal to the axis is a smaller fraction of the sphere radius at larger expansion ratios and viscosity ratios, for which the interior stagnation circle lies farther forward. At $\epsilon = 0.1$ and $\mu_1/\mu_2 = 1$ (figure 2*b*), on the other hand, material lines remain in the shape of an umbrella at large times: circulation within the spherical vortex is slow when compared to the rate of inflow due to expansion of the sphere. Qualitatively similar particle motions, again giving the thin umbrella shape to material surfaces, are obtained at $\epsilon = 0.20$, $\mu_1/\mu_2 = 0$. When ϵ is so large that there

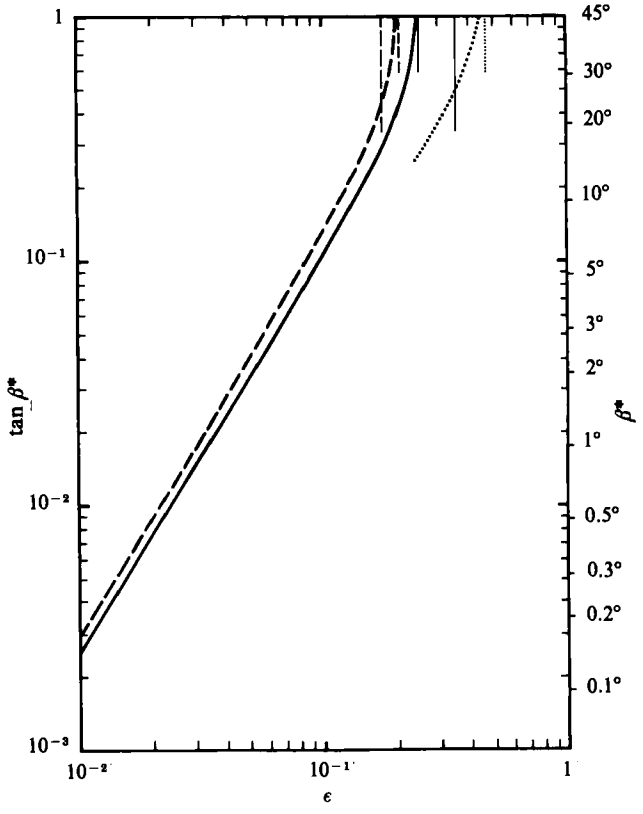

FIGURE 6. The angle β^* subtended at the axis by the dividing particle path far ahead of the thermal in the expanding coordinate frame, as a function of expansion rate for $\mu_1/\mu_2 = 0$ (solid curve) and $\mu_1/\mu_2 = 1$ (dashed curve). Longest vertical lines at the top of the figure indicate corresponding values of ϵ above which there is no interior circulation about a stagnation circle. Short vertical lines are values of ϵ to which the curves asymptote and above which there are no rear stagnation points ($\beta^* \to \infty$). The dotted curves show Turner's (1964) results for inviscid thermals.

is no closed circulation at all within the sphere in expanding coordinates (figure 3), neither the dye ring nor the umbrella cap are formed: the material surfaces then outline, at large times, a tapered compact blob. When ϵ is greater than both ϵ' and ϵ^* all particle paths approach the single stagnation point on the axis a short distance above the centre of the sphere.

4. Strain and mass transport in the environment

In a non-expanding coordinate system at rest in the fluid far from the sphere, the exterior streamfunction (2) for Stokes flow becomes

$$\psi_2 = \tfrac{1}{2}Ua^2 \sin^2\theta\left[\left(\frac{r}{a}-\frac{a}{r}\right)\left(\frac{\mu_2+\frac{3}{2}\mu_1}{\mu_2+\mu_1}\right)+\frac{a}{r}\right]. \tag{14}$$

Velocities decay as r^{-1}, where r is the distance from the centre of the sphere. Hence, integration over time of the vertical component of velocity for a given fluid particle during the passage of a sphere (whether expanding or not) gives an unbounded displacement. Equivalently, the distortion of material surfaces as shown in

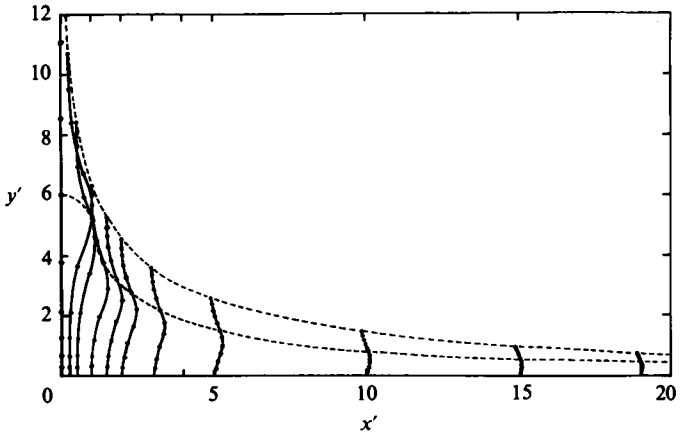

FIGURE 7. Displacements of fluid particles relative to axes (x', y') at rest during the passage of a non-expanding sphere with $\mu_1/\mu_2 = 0$. Particles initially lay on a horizontal line through the axis of motion and ten radii ahead of the sphere ($y' = 0$, $y_0 = 10$). Scales are in sphere radii. Dots show particle positions at the times corresponding to the dots in figure 4. Broken lines connecting simultaneous positions correspond to the material lines of figure 4. Displacements are unbounded in time.

figures 1–4 does not asymptote toward a well-defined 'total drift function', and the drift mass (found from the volume under the drift curve) is infinite. Similarly, the mass flux through any horizontal plane, $2\pi\rho\psi_2(r\to\infty)$, and the added-mass m_a, defined as

$$m_a = \frac{2\pi\rho}{U^2}\iiint_D (v_r^2 + v_\theta^2)\, r^2\, \mathrm{d}r\, \mathrm{d}\theta\, \mathrm{d}\phi$$

(where D is the unbounded domain outside the sphere and v_r, v_θ are velocity components relative to a coordinate frame at rest), are infinite. These results are obvious but emphasize the magnitude of vertical mass transport induced in viscous fluids by the passage of rigid bodies and bubbles, as well as expanding thermals with small Reynolds numbers.

Particle positions relative to the coordinate frame at rest for a non-expanding sphere with $\mu_1/\mu_2 = 0$ are plotted in figure 7. Similar computations of displacements induced by expanding thermals show larger displacements at large times as a result of the increasing sphere radius. At large distances from the axis, vertical displacements (δ) decay only slowly with distance ($\sim x^{-1}$). On the other hand, the strain ($\partial\delta/\partial x$) decreases more rapidly ($\sim x^{-2}$). Rather than computing the strain induced in a given material surface (such as in figure 7) as a function of x and t, it is of interest to consider a horizontal plane and find the angle between this plane and all intersecting material surfaces that, at a given instant in time, have experienced various degrees of distortion (as in figure 4), as though we are looking at a geological structure in which strata have been deformed by a rising spherical mass and then eroded to a horizontal plane. Results are plotted on figure 8 for levels at the top of the sphere ($y = 1$), the centre ($y = 0$), and the bottom ($y = -1$). At $y = 0$, the strain angle decreases from 90° at $x = 1$ to 45° at $x \approx 1.6$. The corresponding curves at $y = 1$ and $y = 0$ for expanding spheres are little different from those shown.

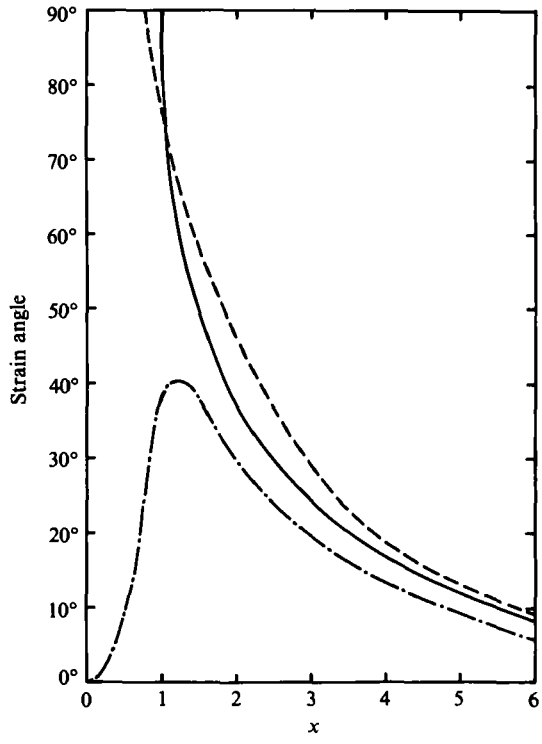

FIGURE 8. The strain angle, $\tan^{-1}(\partial\delta/\partial x)$, as a function of distance in sphere radii normal to the axis of motion, on the three horizontal planes $y = 1$ (–·–·–), $y = 0$ (through the centre of the sphere, ——) and $y = -1$ (– – – –). These results are for a sphere of constant radius.

5. Experimental results

Comparison with the predicted particle motions are provided by laboratory experiments in which hot high-viscosity oil is injected into a large tank of the same oil at room temperature. The experiments were described in I, where the dynamics and motion of the thermals were investigated. Here, the distortion of horizontal dye lines in the tank, and the shapes into which the dyed injected fluid is moulded, are the properties of interest. Additional experiments were carried out in order to extend to smaller Rayleigh numbers the parameter range covered.

5.1. *Conversion of expansion ratio to Rayleigh number*

The semi-empirical relationship (1) can be used to place the computed flow regimes in terms of the Rayleigh number of thermals. Although the dependence of ϵ on Ra was confirmed by experiment only in the range $250 < Ra < 25000$, its form was predicted by a similarity solution for all $Ra \gg 1$. Hence, we assume (cautiously) that (1) holds for $Ra > 10$. Then the numerical results in figures 1, 2 and 3 correspond to $Ra \approx 1736$, 156 and 27, respectively. Similarly, the Rayleigh numbers Ra' below which no rear stagnation points are predicted are $Ra' = 24.8$ for $\mu_1/\mu_2 = 0$ and $Ra' = 36.5$ for $\mu_1/\mu_2 = 1$. A closed interior circulation should not exist at $Ra^* \leqslant 12.5$ ($\mu_1/\mu_2 = 0$) or $Ra^* \leqslant 50$ ($\mu_1/\mu_2 = 1$), while an obvious dye ring is predicted to form for all viscosity contrasts at Rayleigh numbers greater than about 200–300.

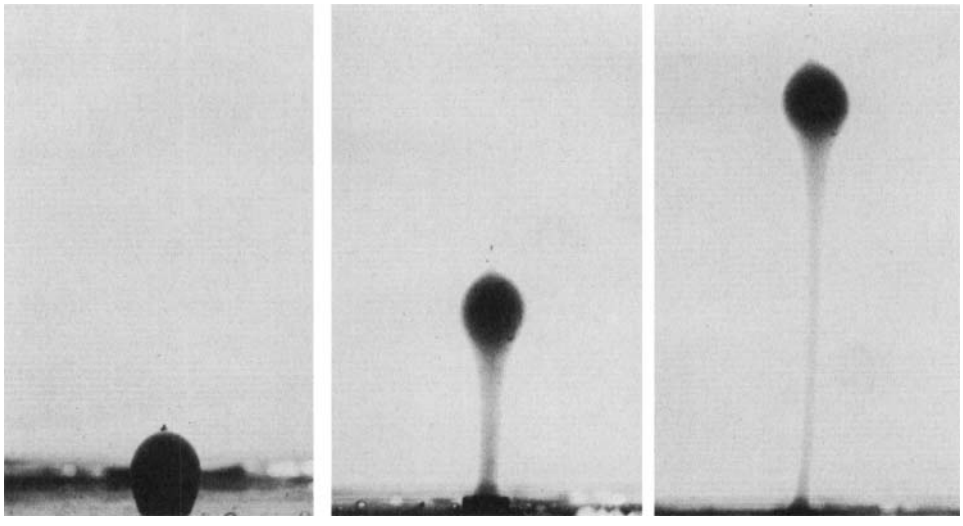

FIGURE 9. Photographs of three stages in the rise of a laboratory thermal in 'Hyvis 30' oil. Hot dyed oil (5 cm^3) was injected at the source and left to rise. Outer viscosity was 1.8×10^3 cm^2 s^{-1}, $\Delta T_0 = 48.7$ °C, $Pr = 1.8 \times 10^6$, $Ra = 80$, $Re = 7.1 \times 10^{-6}$. For scale, the diameter of the dyed blob in the first frame is 2.1 cm. Dimensions of the tank of oil were $67 \times 67 \times 30$ cm deep. Frames were taken at times 120 s, 1260 s, and 3640 s after injection.

5.2. *Shaping of dye within thermals*

The smallest Rayleigh number achieved in the experiments is $Ra = 80$ (with a Reynolds number $Re = 7.1 \times 10^{-6}$). In this case (figure 9), the injected hot fluid containing dye rose away from the source at the base of the tank as a tapered blob. It remained as a compact tear-drop at large times, with a narrow stem that continued to stretch and thin with time. In this case, the heat is expected to be contained in a spherical volume much greater than the dyed blob. The base of the tank is likely to influence such thermals as they require a very long time to distance themselves from their source. The expansion rate given by (1) is $\epsilon \approx 0.14$. Although the temperature difference was initially 48 °C (and $\mu_1/\mu_2 \approx 0.026$), the similarity solution in I predicts that this will have decreased to 5 °C ($\mu_1/\mu_2 \approx 0.7$) once the thermal has risen a distance of three initial diameters. Hence the expansion rate is only slightly smaller than the value ($\epsilon \approx 0.18$) above which no interior recirculation is predicted. The very long time required for material surfaces to approach their final shape under these conditions (see figures 2(*b*), 3) as well as an unknown initial period of adjustment towards self-similar flow must also be considered. However, the compact tapered dye blob is consistent with the kinematic model.

At a Rayleigh number $Ra = 182$ ($\epsilon \approx 0.093$), the injected dye forms a thin umbrella-shaped cap (figure 10). Most of the dyed fluid is confined to a torus with thin, elongated and inclined cross-section. This shape compares well with that predicted for $\epsilon \approx 0.1$, $\mu_1/\mu_2 \approx 1$ (figure 2*b*). At a Rayleigh number $Ra = 312$ ($\epsilon \approx 0.07$), the axisymmetric torus of dyed fluid is a more obvious feature of the flow (figure 11) and can be seen clearly in plan view (figure 12). The thin spherical cap, forward stagnation point, and thin axial stem of dye extending all the way to the source are all visible in these experiments. Note that the intermediate stages in the moulding of the dyed fluid shown in figures 9–11 result from an approximately

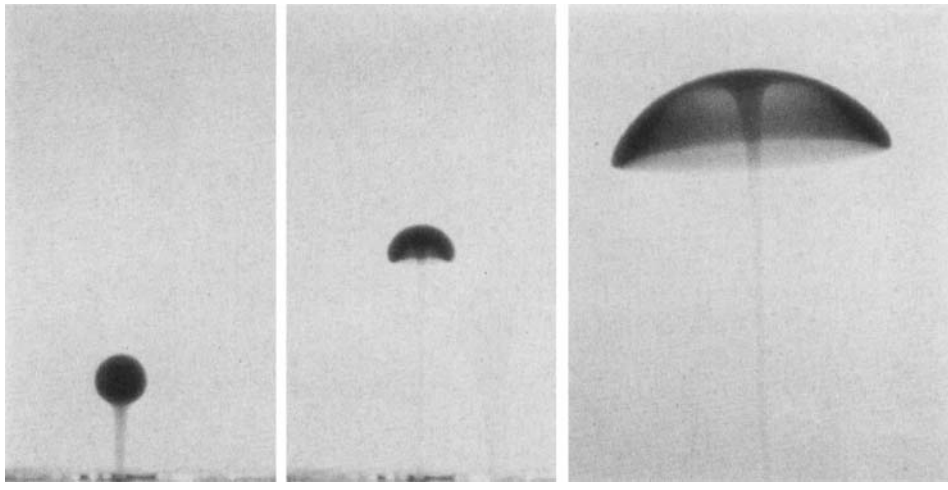

FIGURE 10. Photographs showing the shape into which dye is moulded in a thermal with $V_0 = 11.2\,\mathrm{cm}^3$, $\Delta T_0 = 48.7\,^\circ\mathrm{C}$, $Ra = 182$ and $Re = 1.6 \times 10^{-5}$. The fluid has a Prandtl number $Pr = 1.8 \times 10^6$. For scale, the diameter of the dyed blob in the first frame is 2.8 cm and the third frame is enlarged about three times. Container as in figure 9. Frames were taken at times 425 s, 1560 s, and 4800 s after injection.

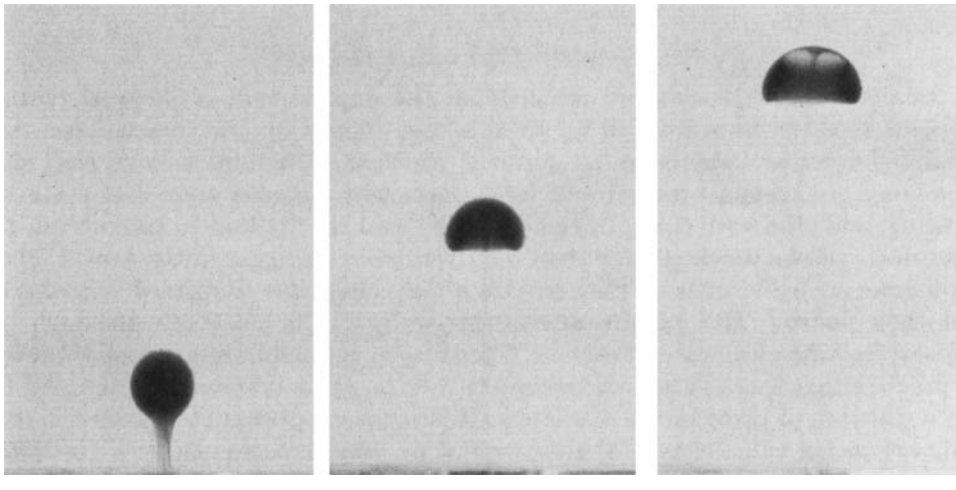

FIGURE 11. Photographs showing the shape of dyed fluid in a thermal with $V_0 = 20.5\,\mathrm{cm}^3$, $\Delta T_0 = 48.7\,^\circ\mathrm{C}$, initial viscosity ratio $\mu_1/\mu_2 = 0.024$, $Ra = 312$, $Re = 2.8 \times 10^{-5}$ in 'Hyvis 30'. Container as in figure 9. The dye blob in the first frame has diameter 3.5 cm. Photographs were taken at times 120 s, 600 s, and 1800 s after injection.

self-similar evolution of the flow. The outline of the dye at intermediate to large times can therefore be compared to the computed shapes inside the spherical vortex of initially horizontal material surfaces: the differing initial conditions of a spherical surface intersecting the source and a planar surface above the thermal prevent comparison at only short times.

At large Rayleigh numbers the dye ring is centred farther behind the forward stagnation point and its cross-section is elongated more nearly parallel to the axis

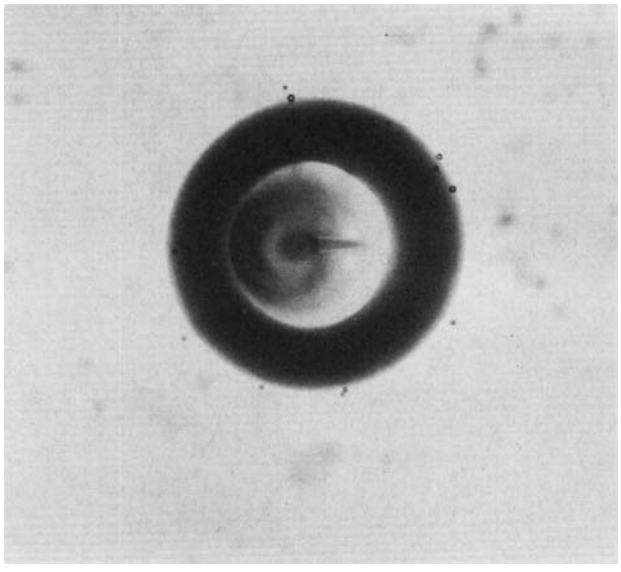

FIGURE 12. A plan view of the thermal in figure 11, taken 1200 s after injection. The dye ring and thin vertical stem can be seen. The source lies on the base of the tank beneath the centre of the ring.

(figure 13). Lines of dye placed across the tank at various heights before injection of the thermals (see I) show a pattern of displacement of the environment entirely consistent with that computed from the model. On the other hand, quantitative comparison of the vertical transports is not possible because the dye lines could not be positioned to pass precisely through the axis of motion for thermals (which generally do not follow an absolutely perfect vertical line from the source). Hence, dye lines generally do not meet the forward stagnation point and are advected around the near or far side of each thermal. They are therefore displaced slightly smaller distances than predicted by the numerical solutions. Some influence of the finite width of the tank (40 cm) is also detectable: dye lines 10–15 cm from the axis are advected a small distance downward during the rise of a thermal.

Similar distortions of dye lines in the environment are seen for the case of isothermal, non-expanding bubbles of less dense oil (figure 14). Comparison with figure 4 shows that these observations too, are well described by computed shapes of material surfaces. Other experiments showing the displacement of marked horizontal surfaces (rather than lines) in non-diffusive Stokes flow are described by Ramberg (1981), who used putties of differing densities in a high-speed centrifuge. However, those flows were strongly influenced by the small depth of material used.

6. Conclusions

A simple kinematic model for the particle motions in and around an expanding thermal with small Reynolds number successfully predicts the shapes into which passive tracers are moulded by the flow. Both model predictions and laboratory observations of the rise of hot, dyed blobs in viscous oil show that injected dyed fluid remains as a compact blob with a tapering stem if the Rayleigh number is small ($Ra < 80$). At intermediate Rayleigh numbers ($Ra \sim 100$) the dye forms into a thin

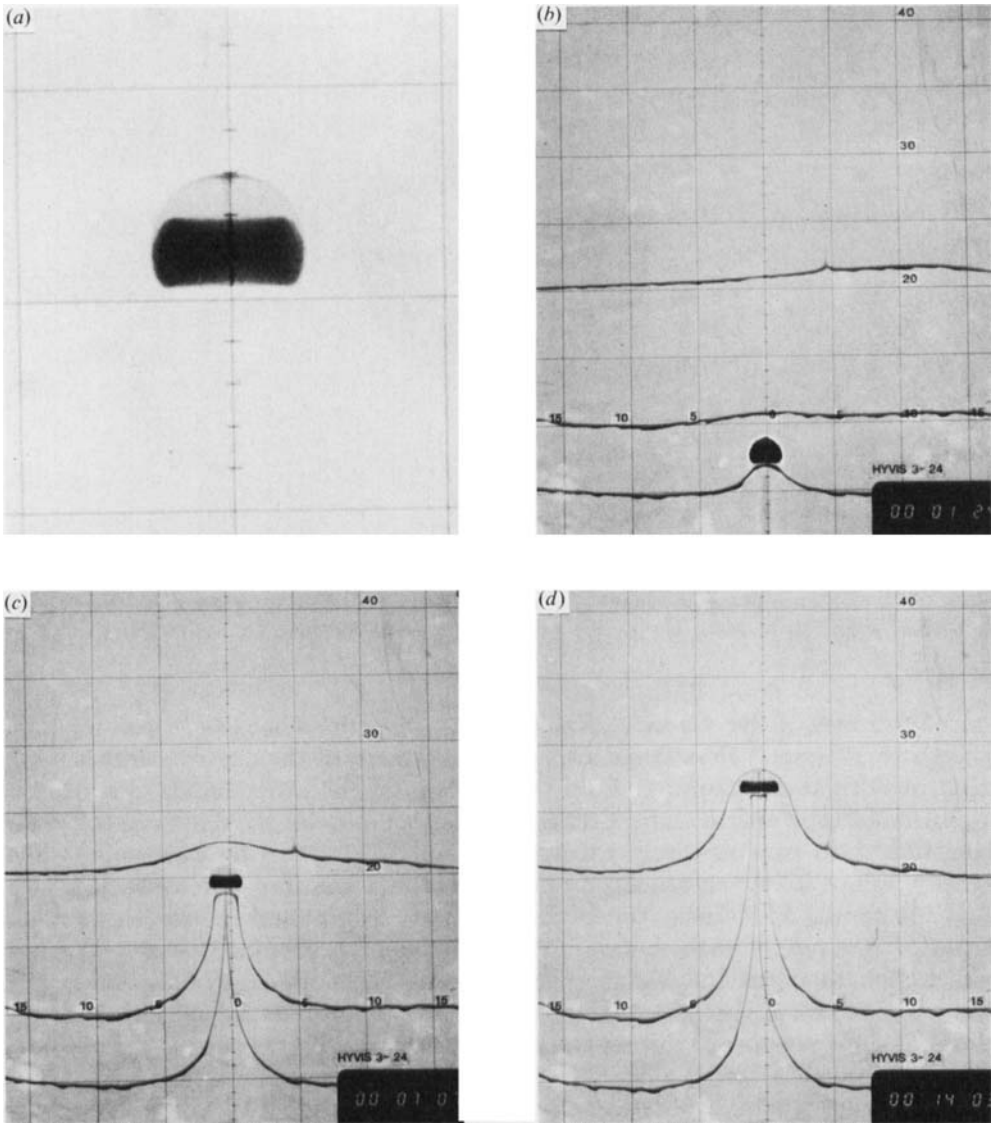

FIGURE 13. Shadowgraph images of two thermals in 'Hyvis 3' oil, both with $V_0 = 2.4$ cm^3, $\Delta T_0 = 70$ °C, initial viscosity contrast $\mu_1/\mu_2 = 0.0125$, $Ra = 1.65 \times 10^3$ and $Re = 1.8 \times 10^{-3}$. The Prandtl number is 1.2×10^5. In the first frame a larger concentration of dye in the injected hot oil used to create the thermal makes visible the thin spherical cap and forward stagnation point. Most dye is confined to the dye ring at large times, shown when the cap is 33 cm above the source. Nearly horizontal dye lines in the second experiment (second-fourth frames) pass close to the axis of motion and are entrained into the thermal. A 5 cm square grid is drawn on the shadowgraph screen. Dimensions of container were $40 \times 40 \times 70$ cm deep.

mushroom- (or umbrella-) shaped cap and a thin axial stem. At large Rayleigh numbers ($Ra > 200$) most of the dye is, at large enough times, confined to an axisymmetric torus or dye ring of ever-increasing radius and decreasing cross-sectional area. Buoyancy, on the other hand, is assumed to remain evenly distributed throughout an encompassing spherical volume that rises with Stokes terminal velocity.

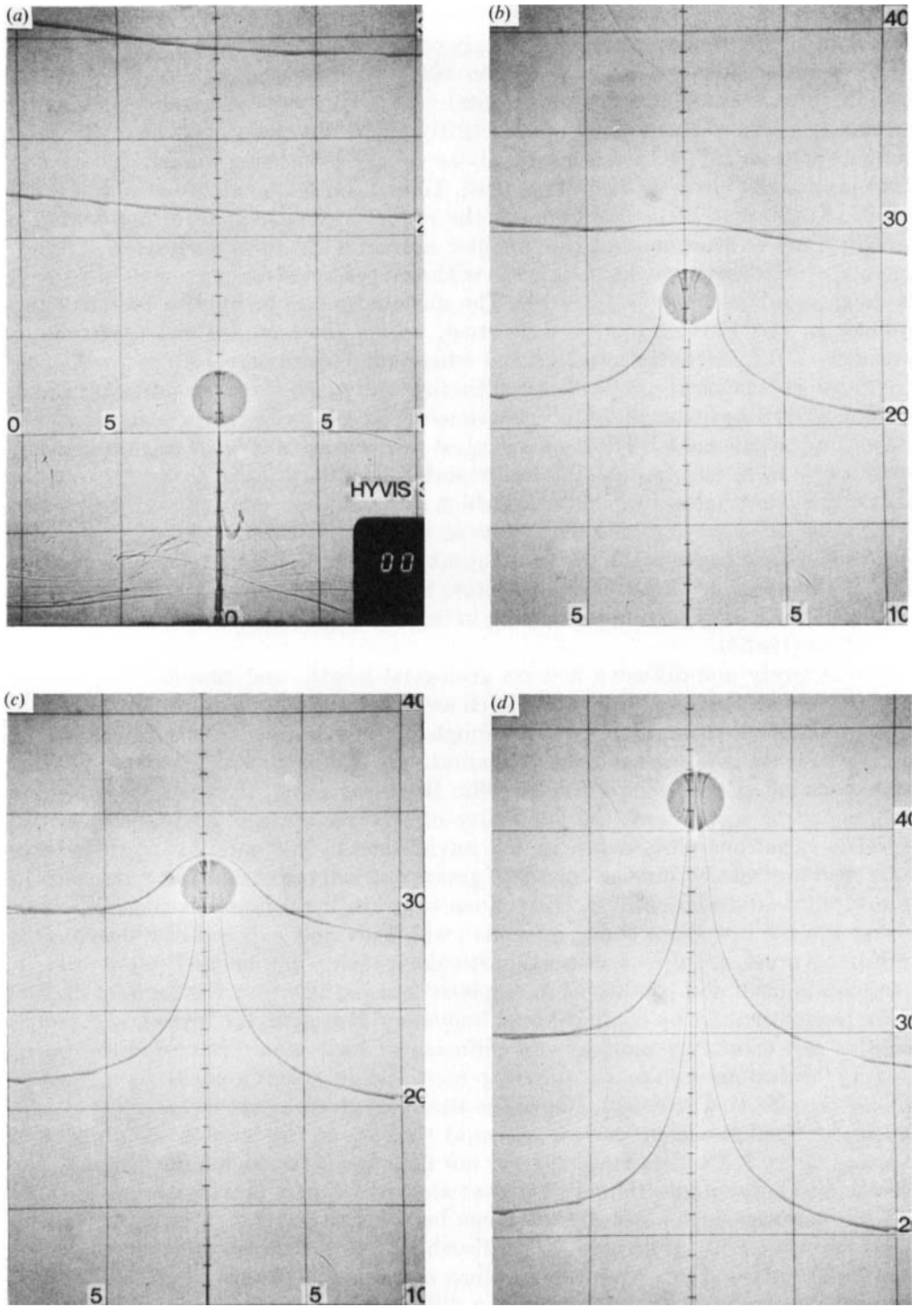

FIGURE 14. Shadowgraph images of an isothermal, non-expanding bubble as it passes through passive dye lines. $\Delta\rho = 0.0106$ g cm^{-3}, outer viscosity 90 cm^2 s^{-1}, $V = 11.3$ cm^3, $\mu_1/\mu_2 = 0.09$, $Re = 2.0 \times 10^{-3}$. Container as in figure 13. Although the fluids are completely miscible and interfacial tension is negligible, the bubble does not entrain surrounding fluid and moves at a constant velocity.

Although the model will not be quantitatively accurate for Reynolds numbers greater than one, it does explain previously observed distributions of passive tracers within laminar thermals with $Re \sim 1$ to 100. For example, an unstable thermal boundary layer above a heated horizontal plate gives rise to 'mushroom-shaped' thermals (Sparrow, Husar & Goldstein 1970). These thermals must have Rayleigh numbers of order 10^3 (the density anomaly and lengthscale being comparable to those of the marginally unstable boundary layer). They show clear evidence of recirculation within the thermal, while dye entering the convective element from the boundary layer appears to pass most of the distance around a spherical surface. Hence, the appearance of these thermals is consistent with that predicted for intermediate-to-large Rayleigh numbers, such as $Ra \sim 10^3$. The model also can be applied to convective motions in the Earth's mantle and crust, where motions are characterized by extremely small Reynolds numbers and where our results may help to predict the distribution of chemical composition within thermally-driven diapirs and their effects on the surrounding material. Large variations of viscosity with temperature are taken into account in the model. The results suggest that if masses of hot, buoyant material break away from an often-postulated unstable boundary layer at the base of the mantle then that hot source material (which may also be chemically or isotopically distinct) will become confined to a torus as it rises in a thermal. The torus should form in this case because the Rayleigh number for the thermals must be similar to that for the boundary layer and is therefore likely to be of order 10^3. Each thermal will also cause a large amount of stirring in the fluid layer. This example is discussed in Griffiths (1986*b*).

An effectively non-diffusive flow on geological length- and timescales is motion driven by a compositional buoyancy, such as the ascension of salt domes. These are isothermal masses that push upward through the surrounding crust and deform the geological strata in a manner at least qualitatively similar to that predicted here for non-expanding spheres (Schwerdtner 1982; Ramberg 1981), though differences can be expected to result from the proximity of the free surface, and from effective viscosity variations with depth in the environment. The consequent doming of impermeable strata within the crust is of great practical importance as it forms traps for natural gas and oil reservoirs. Distortions, or strain, in the immediate surroundings of large granite intrusions called 'plutons', which are now exposed at the surface of the Earth's crust, are also of interest, particularly if they can be used to infer details of the mechanism and conditions of emplacement. In this case too the motion was driven predominantly by compositional buoyancy. However, the intruding material was also hot (probably molten) and diffusion of heat would have induced large viscosity variations in the surrounding rock. Large stresses could have further reduced the effective viscosity. Hence the strain, as given by the dip angle of strata, may be confined to a more narrow region at the edge of the buoyant material than is seen in figure 8. Particle motions have not been found for such a flow, though the velocity of a hot, compositionally buoyant and rigid sphere moving through a fluid with temperature-dependent viscosity has been investigated by Marsh & Kantha (1978), Morris (1982), Ribe (1983) and Marsh (1984). Similarly, solutions have not been found for the flow or particle motions about a sphere that is driven by both thermal (diffusing) and compositional (non-diffusing) buoyancies. Some aspects of the latter case are discussed in Griffiths (1986*c*).

Mr R. Wylde-Browne is thanked for his assistance with preparation of photographs and figures.

REFERENCES

BATCHELOR, G. K. 1967 *An Introduction to Fluid Dynamics*. Cambridge University Press.

DARWIN, C. 1953 Note on hydrodynamics. *Proc. Camb. Phil. Soc.* **49**, 342–354.

GRIFFITHS, R. W. 1986*a* Thermals in extremely viscous fluids, including the effects of temperature-dependent viscosity. *J. Fluid Mech.* **166**, 115–138.

GRIFFITHS, R. W. 1986*b* Dynamics of mantle thermals with constant buoyancy or anomalous internal heating. *Earth Planet. Sci. Lett.* (in press).

GRIFFITHS, R. W. 1986*c* The differing effects of compositional and thermal buoyancies on the evolution of mantle diapirs. *Phys. Earth Planet. Inter.* (submitted).

KOJIMA, M., HINCH, E. J. & ACRIVOS, A. 1984 The formation and expansion of a toroidal drop moving in a viscous fluid. *Phys. Fluids* **27**, 19–32.

LAMB, H. 1932 *Hydrodynamics*. Dover.

LIGHTHILL, M. J. 1956 Drift. *J. Fluid Mech.* **1**, 31–53.

MARSH, B. D. 1984 Mechanics and energetics of magma formation and ascension. In *Explosive Volcanism: Inception, Evolution and Hazards*, pp. 67–83. Washington: National Academy Press.

MARSH, B. D. & KANTHA, L. H. 1978 On the heat and mass transfer from an ascending magma. *Earth Planet. Sci. Lett.* **39**, 435–443.

MAXWELL, J. C. 1870 On the displacement in a case of fluid motion. *Proc. Lond. Math. Soc.* **3**, 82–87.

MORRIS, S. 1982 The effects of a strongly temperature dependent viscosity on slow flow past a hot sphere. *J. Fluid Mech.* **124**, 1–26.

MORTON, B. R. 1960 Weak thermal vortex rings. *J. Fluid Mech.* **9**, 107–118.

RAMBERG, H. 1981 *Gravity, Deformation and the Earth's Crust* 2nd edn. Academic.

RIBE, N. M. 1983 Diapirism in the Earth's mantle: experiments on the motion of a hot sphere in a fluid with temperature dependent viscosity. *J. Volcanol. Geotherm. Res.* **16**, 221–245.

SCHWERDTNER, W. M. 1982 Salt rocks as natural analogues of Archaean gneiss diapirs. *Geol. Rundschau*, **71**, 370–379.

SCORER, R. S. 1957 Experiments on convection of isolated masses of buoyant fluid. *J. Fluid Mech.* **2**, 583–594.

SCORER, R. S. 1978 *Environmental Aerodynamics*. John Wiley.

SPARROW, E. M., HUSAR, R. B. & GOLDSTEIN, R. J. 1970 Observations and other characteristics of thermals. *J. Fluid Mech.* **41**, 793–800.

TURNER, J. S. 1957 Buoyant vortex rings. *Proc. Roy. Soc.* A **239**, 61–75.

TURNER, J. S. 1964 The flow into an expanding spherical vortex. *J. Fluid Mech.* **18**, 195–208.

TURNER, J. S. 1973 *Buoyancy Effects in Fluids*. Cambridge University Press.

YIH, C.-S. 1985 New derivations of Darwin's theorem. *J. Fluid Mech.* **152**, 163–172.